Calculation of Global Atlas of Siting Parameters

Larsén, Xiaoli Guo; Davis, Neil; Hannesdóttir, Ásta; Kelly, Mark; Olsen, Bjarke; Floors, Rogier; Nielsen, Morten; Imberger, Marc

Publication date:
2021

Document Version
Publisher's PDF, also known as Version of record

Citation (APA):
Larsén, X. G., Davis, N., Hannesdóttir, Á., Kelly, M., Olsen, B., Floors, R., Nielsen, M., & Imberger, M. (2021). *Calculation of Global Atlas of Siting Parameters*. DTU Wind Energy. DTU Wind Energy E No. E-Report-0208

DTU Wind Energy E-Report-0208

Calculation of Global Atlas of Siting Parameters

Xiaoli Guo Larsén, Neil Davis, Ásta Hannesdóttir, Mark Kelly, Bjarke Olsen, Rogier Floors, Morten Nielsen, Marc Imberger

DTU Wind Energy
Department of Wind Energy

DTU Wind Energy, Risø Campus,
Technical University of Denmark, Roskilde, Denmark

February 2021

Author: Xiaoli Guo Larsén, Neil Davis, Ásta Hannesdóttir, Mark Kelly, Bjarke Olsen, Rogier Floors, Morten Nielsen, Marc Imberger
Title: Calculation of Global Atlas of Siting Parameters
Department: DTU Wind Energy

DTU Wind Energy E-Report-0208
February 9, 2021

ISSN:978-87-93549-76-0

Abstract (max. 2000 char)

Here is some abstract text...

Contract no:
XX-XXXXX

Project no: EUDP 64018-0095

Sponsorship:

Cover:-

Tables: 0
Figures: 11
References: 26

Technical University of Denmark
Frederiksborgvej 399
4000 Roskilde
Denmark
Tel. +4546775024
xgal@dtu.dk
www.vindenergi.dtu.dk

Contents

1 Introduction

This is the first version of the GASP technical report on the calculation of a series of siting parameters, including the 50-year winds and turbulence intensity at three heights (50 m, 100 m and 150 m). This report documents the methodologies behind the calculations of a variety key siting parameters. We also describe how the massive, global calculation at a resolution of 250 m is done.

2 Generalized Extreme wind climate

In this section we describe the process and steps of obtaining the Generalized extreme wind climate (GEWC). In this process the wind data is corrected for the influence of orography and surface characteristics that influence the wind flow near the surface. Further we apply the spectral correction method to correct for the underestimation of extreme winds from mesoscale simulations. The GEWC is calculated globally on a coarse grid with the same grid resolution as the reanalysis data set chosen for GASP. The GEWC serves as input for calculating the 50-year extreme wind output at a finer grid.

2.1 CFSR data

In this project we used the Climate Forecast System Reanalysis (CFSR) data (Saha et al., 2010) covering a 31-year period from 1979 to 2011. The CFSR data set provides various variables with an hourly temporal resolution and global coverage with a 0.3125° grid resolution. Here we use the longitudinal and meridianal components of wind at 10 m to find annual wind speed maxima per wind speed sector, with 12 wind speed sectors, centered around 0°, 30°, ... , 300°, 330°. Figure 1 shows an example year of CFSR annual maximum westerly wind speed.

The choice of using the CFSR data was based on the study where a number of the most-used reanalysis data are examined for the purpose of calculating the 50-year wind. The reanalysis includes CFDDA, MERRA, ERA5 and CFSR. The studied areas are South Africa and Europe where we have measurements for validation. This study shows that CFSR outperforms the other datasets using our method for the extreme wind calculation (Larsén et al., 2019). This study is attached as Appendix A (Finding the suitable reanalysis data for GASP).

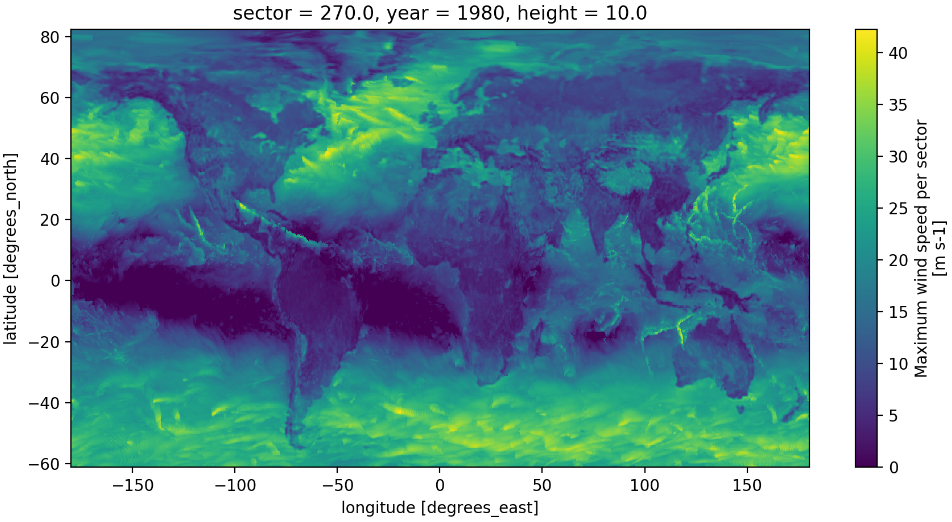

Figure 1: Annual maximum wind speed from the CFSR data set.

Further we use the u- and v-component momentum fluxes to calculate the friction velocity:

$$u_* = (\overline{u'w'}^2 + \overline{v'w'}^2)^{1/4} \tag{1}$$

2.2 Gumbel extreme wind distribution

The 50-year extreme winds are estimated with a probability weighted moment (PWM) method (Abild, 1994; Larsén and Mann, 2009), where we assume the annual maxima to follow a Gumbel distribution:

$$F(U) = \exp\left(-\exp\left(-\left(\frac{U_{\max} - \beta}{\alpha}\right)\right)\right) \tag{2}$$

where $U_{\max}$ is the annual wind speed maximum per grid point. The Gumbel distribution parameters α and β are estimated with:

$$\alpha = \frac{2b_1 - b_0}{\ln 2} \tag{3}$$

$$\beta = b_0 - \gamma\alpha \tag{4}$$

where $\gamma \approx 0.5772...$ is Euler's constant, b_0 is the the first PWM which corresponds to the average annual maximum, and b_1 is the the second PWM given by

$$b_1 = \frac{1}{n}\sum_{i=1}^{n}\frac{i-1}{n-1}U_{\max_i}. \tag{5}$$

By combining the exceedance probability $1/T = 1 - F(U_t)$ and the Gumbel distribution (eq.2) we can estimate the T-year wind speed with

$$U_T = -\alpha \ln\left(\ln\left(\frac{T}{T-1}\right)\right) + \beta \tag{6}$$

where $T = 50$ is the 50-year return period.

2.3 Roughness length for generalization use

For the purpose of generalization, two different methods are used to calculate the roughness length, one over land and one over water. The roughness length over land is based on the logarithmic wind profile:

$$z_0 = h\left\langle \exp\left(-\frac{\kappa U_{\max}}{u_*}\right)\right\rangle \tag{7}$$

where $h = 10\,m$ is the height above ground, $\kappa = 0.4$ is the Von Kármán constant, u_* is the friction velocity corresponding to the time of $U_{\max}$ and $\langle ... \rangle$ denotes the ensemble average over the 31 annual maxima.

For estimating the roughness length over water a combination of the logarithmic wind profile and the Charnock formulation is used. The first step is to estimate the friction velocity by finding the roots of the following equation:

$$\frac{u_*}{\kappa}\ln\left(\frac{hg}{a_c u_*^2}\right) - U_{50} = 0 \tag{8}$$

where $a_c = 0.05$ is the Charnock coefficient chosen here for high wind speeds, $g \approx 9.81\,ms^{-2}$ is the gravitational acceleration and U_{50} is the estimated 50-year wind. The second step is to input the estimated u_* in the Charnock's relation:

$$z_0 = a_c\frac{u_*^2}{g} \tag{9}$$

Note, these roughness lengths over water are artificial; they are derived from extreme wind values in order to secure a rather smooth transition of land-sea roughness length change, as useful for the generalization approach.

2.4 Generalization

Topography effects influencing modelled winds are removed through a process called wind climate generalization, which is a WAsP function (e.g. Troen and Petersen (1989), Badger et al. (2014)). A generalized wind climate describes the winds over flat terrain with uniform surface roughness. The flow perturbation caused by gradients in ground elevation and in surface roughness are considered separately in the generalization. These perturbations are modelled with LINCOM, which is a linearized flow model for neutrally stationary flow over terrain. A detailed description and derivation of the basic equations behind the LINCOM model may be found in Astrup et al. (1996).

The local flow perturbation of wind direction due to the changes in ground elevation is defined by

$$\delta\theta_{\text{oro}} = \theta_{\text{flat}} - \theta_R \tag{10}$$

where θ_{flat} is the wind direction estimated for flat terrain and θ_R is the reanalysis wind direction. For the wind speed we apply generalization factors, where the orography factor accounting for upstream changes in ground elevation is given by

$$F_{\text{oro}} = \frac{|U_R|}{|U_{\text{flat}}|} \tag{11}$$

where $|U_R|$ is the wind speed from the reanalysis data set, and $|U_{\text{flat}}|$ is the wind speed estimated for flat terrain. The roughness factor accounting for upstream changes in surface roughness is defined by

$$F_{\text{rou}} = \frac{|U_{\hat{z}_0}|}{|U_R|} \tag{12}$$

where $|U_{\hat{z}_0}|$ is the estimated wind speed for a uniform upstream roughness length $\hat{z}_0$ that is a function of the wind direction.

2.5 Spectral correction method

The extreme wind speeds from mesoscale simulations are underestimated due to the smoothing effect resulting from the effective model temporal and spatial resolution. The spectral correction method (SCM) was developed by Larsén et al. (2012) to improve the estimation of extreme wind speed using mesoscale data. This method has been implemented in WAsP Engineering 4 in connection with global CFDDA data and a spectrum from limited measurements at site. It is validated using measurements from a number of sites across several continents in Hansen et al. (2016). This method has been applied to reanalysis data for the South Africa Wind Atlas using a spectral model, where it was evaluated with more than 72 stations across South Africa; satisfactory results were found Larsén and Kruger (2014).

Investigating wind speed from mesoscale simulations in the spectral domain reveals how the energy level in the mesoscale range is underestimated when compared to measured wind speed. The slope of the mesoscale wind speed spectra is steeper than for the measured wind speed spectra for frequencies that are higher than a certain frequency value f_c. This frequency is usually found to be at the order of 1 day^{-1} at the mid latitudes. One important step of the SCM is to estimate a hybrid spectrum, where the slope of the mesoscale spectrum is corrected, or given the same slope as wind speed measurement spectrum at frequencies higher that f_c.

The basic assumption behind the SCM is that the annual wind speed maxima (U_{max}) follow a Poisson process with a high threshold. This process may be simplified with a Guassian process, where the annual wind speed maxima may be expressed as

$$\tilde{U}_{\text{max}} = \overline{U} + \sqrt{m_0}\sqrt{2\ln\left(\frac{1}{2\pi}\sqrt{\frac{m_2}{m_0}}T_0\right)} \tag{13}$$

where $\overline{U}$ is the mean wind speed, T_0 is the basis period of one year and m_i is the ith spectral moment defined by

$$m_i = 2\int_0^{\infty} f^i S(f)\,df \tag{14}$$

where f is the cyclic frequency and $S(f)$ is the spectrum of the wind speed. We can use the annual wind speed from the Gaussian process (13) to define the spectral correction factor:

$$F_{\mathrm{sc}} = \frac{\tilde{U}_{\mathrm{max}}^{\mathrm{hybrid}}}{\tilde{U}_{\mathrm{max}}^{\mathrm{meso}}} \tag{15}$$

where $\tilde{U}_{\mathrm{max}}^{\mathrm{hybrid}}$ is estimated from the hybrid spectrum and $\tilde{U}_{\mathrm{max}}^{\mathrm{meso}}$ is estimated directly from the CFSR wind speed. Here we used 5 years long CFSR wind speed time series to estimate F_{sc}. Figure 2 shows an example of CFSR wind speed spectrum in the mid-latitudes in North America and a corresponding hybrid spectrum. Here the frequency $f_c = 0.8\,\mathrm{day}^{-1}$ is chosen as the default frequency value, where the hybrid spectra is given the same slope as spectra of measured wind speed.

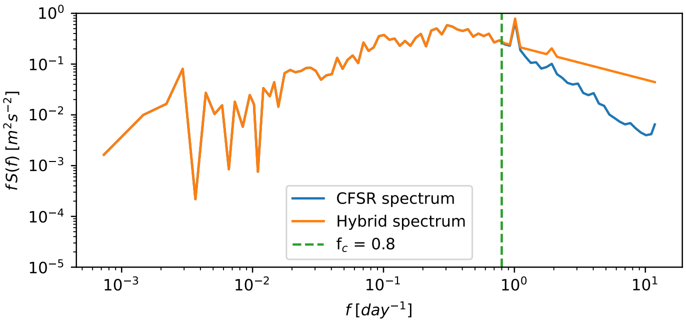

Figure 2: The spectrum of a 5-year CFSR wind speed time series and the corresponding hybrid spectrum at a random grid point in North America. The hybrid spectrum is corrected for $f > 0.8\,\mathrm{day}^{-1}$.

When estimating F_{sc} on a global scale it was found that using $f_c = 0.8\,\mathrm{day}^{-1}$ was not appropriate in areas where convective conditions are frequently observed. The wind speed spectra at such location generally have their highest energy content at frequencies higher than $1\,\mathrm{day}^{-1}$. Figure 3 shows an example of the spectrum and the corresponding hybrid spectrum at a random grid point in the Amazonas region. It may be seen that using $f_c = 0.8\,\mathrm{day}^{-1}$ results in a hybrid spectrum with lower energy content than the corresponding CFSR spectrum for frequencies $f_c < f < 5\,\mathrm{day}^{-1}$.

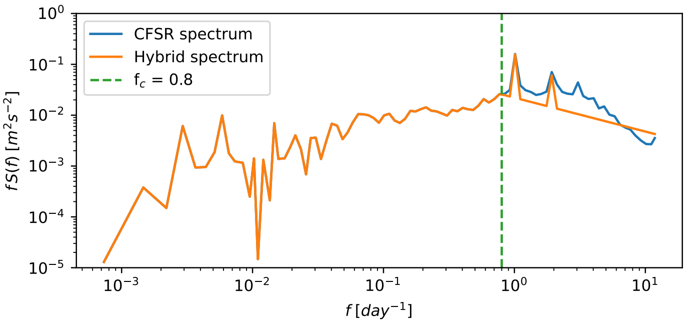

Figure 3: The spectrum of a 5-year CFSR wind speed time series and the corresponding hybrid spectrum at a random grid point in the Amazonas area. The hybrid spectrum is corrected for $f > 0.8\,\mathrm{day}^{-1}$.

To avoid this problem, the spectral correction algorithm was modified to handle regions with frequent convective conditions. In the algorithm f_c is given three possible values $f_c = (0.8, 1.3, 2.2)$, where the first is used as a default. Further we define three corresponding test frequencies $f_t = (1.0, 1.5, 2.5)$. If $S(1.0)_{hybrid} > S(1.0)_{CFSR}$, the first value of f_c is kept. Otherwise we use the next value of f_c and repeat the test with the second value of f_t, and so on. It was not necessary to include higher values for f_c. In Figure 4 the hybrid spectrum has been estimated with $f_c = 2.2\,\mathrm{day}^{-1}$.

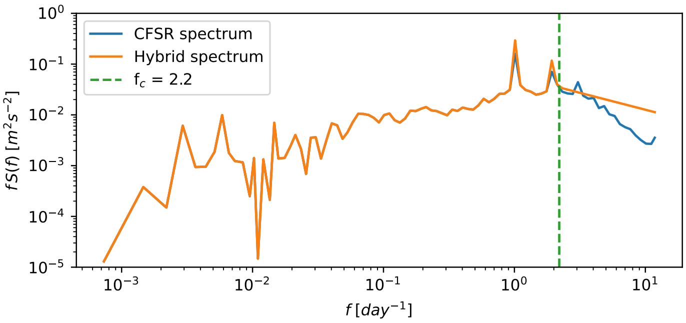

Figure 4: The spectrum of a 5-year CFSR wind speed time series and the corresponding hybrid spectrum at a random grid point in the Amazonas area. The hybrid spectrum is corrected for $f > 2.2\,\mathrm{day}^{-1}$.

3 Air density for extreme winds

In the latest IEC standard (IEC, 2019) one is allowed to correct extreme wind speeds when the air density (ρ) is known, because in general the loads will be lower when the air density is lower. Estimating the air density more accurately at these high wind speeds can thus reduce [comment: or is it increase?] the engineering safety factors inherent in the current approach in the IEC standard. An important criterion is that the dataset can be computed globally based on readily available atmospheric data. To compute air density the pressure P and temperature T are needed. In addition there is a small effect of the amount of water vapour in the air (Floors and Nielsen, 2019).

The recently released ERA5 dataset was used to compute the air density according the methods presented in (Floors and Nielsen, 2019). The ERA5 dataset was chosen because it had lower errors compared to the CFSR reanalysis in modelled ρ when compared to observations of ρ at 77 stations in Germany (Floors and Nielsen, 2019). In addition the presence of the hourly output of the wind speed, U, at 100 m makes it easier to calculate conditional statistics of ρ.

Technically the workflow is very similar as in (Floors and Nielsen, 2019), but the difference is that we want to compute the air density only in cases with high wind speed. In Floors and Nielsen (2019) the means were calculated from rather small files that were averaged in monthly means as available from the Copernicus Data Store. To capture accurately the relation between air density and high wind speeds we need to capture the high wind speed events in more than monthly intervals.

Therefore the full hourly dataset was downloaded. This made processing technically challenging because the 8 years of the data that were used here comprise 4 terabytes of data. An additional complication is that the statistics cannot be calculated in a single pass, because we first have to know the full distribution of wind speeds at each grid point to be able to say what is a high wind speed.

Therefore a script was developed that creates conditional statistics of the full time series of P, T and relative humidity based on the wind speed at 100 m, i.e. the distribution $P(T,P,RH|U)$. In a second step this histogram is then processed to obtain all values above a chosen percentile of wind speed at 100 m. The bin width in the histograms was set to 0.25 m/s.

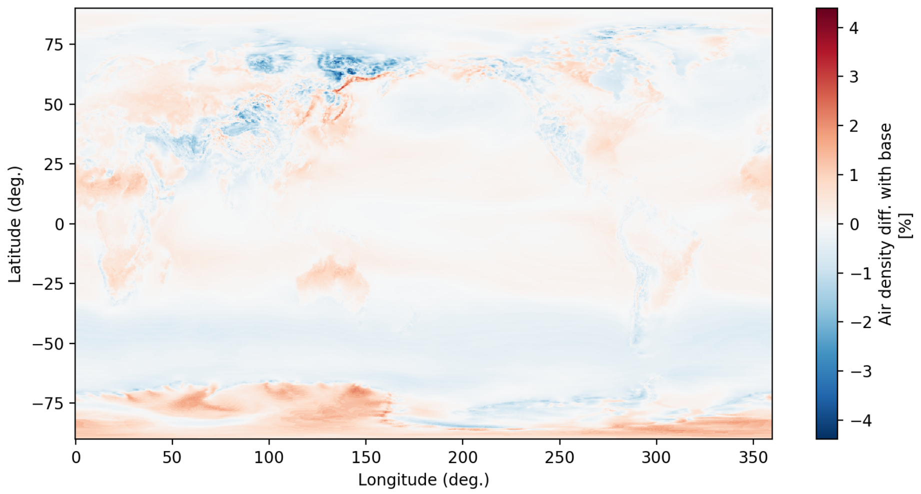

Figure 5: Air density conditioned on the 50th percentile of highest winds compared to the air density considering all wind speeds.

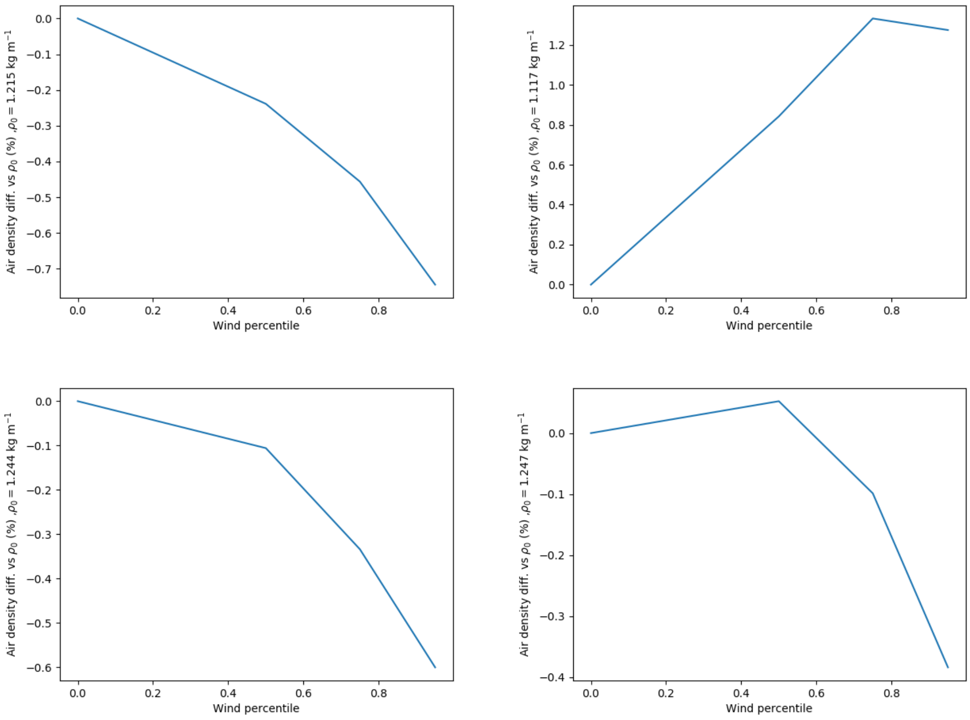

Figure 6: Air density conditioned on the 50th percentile of highests winds compared to the air density considering all wind speeds.

4 Estimation of the turbulence intensity

Two approaches are used for calculating the turbulence intensity $TI = \sigma_u/U$, with U the mean wind speed and σ_u the standard deviation of the along-wind component during a period of T. For boundary-layer flow, T is in the range of 10 min to 1 h. The first approach uses the typical boundary layer turbulence model, the Kaimal model, in connection with inputs of surface roughness lengths; this is described in section 4.1. The second approach is based on terrain-affected shear and stability, through the turbulent kinetic energy budget; this is described in section 4.2.

4.1 Roughness-based turbulence via the Kaimal model

From this approach, we obtained omni-directional as well as the sector-wise distributions of the turbulence intensity and σ_σ with wind speed.

This approach calculates σ_u as the root-mean-square of the integrated power spectrum of u for a range of wind speed from 1 to 50 ms^{-1}, with $z = 50$, 100 and 150 m. Here we use the Kaimal model for u, Eq. 16 (Kaimal et al., 1972):

$$fS_u(f) \quad = \quad \frac{102u_*^2 n}{(1+33n)^{5/3}} \tag{16}$$

where u_* is the friction velocity and n is the normalized frequency $n = fz/U$. The integration is over 1 h^{-1} to 10 Hz.

An important input is the surface roughness length z_0 at a spatial resolution of 250 m, which will be used to obtain u_* as in Eq. 16. This input of z_0 will bring this application to the specific site. For a land site, the roughness is from GWA dataset, called z_{0meso}. It contains 12 sector-wise roughness value, each obtained with a weighting of upwind fetch roughness length up to approximately 10 km. For each site, when calculating the overall TI, an occurrence-frequency weighted value is obtained for z_0. This occurrence-frequency for this site is also provided by the GWA data. When calculating the σ_σ, TI from each sector was calculated and populated with the given occurrence frequency in that sector. On EMD's request, coefficients a and b to a linear fit of TI with U are obtained for the range 5–30 ms^{-1}.

For a water site, the following expressions are used:

$$z_0 = (10\mathrm{m}) \cdot \exp\left(-\kappa/\sqrt{C_d}\right) \tag{17}$$

where

$$C_d = (0.55 + (2.97U_{10}/31.5) - 1.49(U_{10}/31.5)^2) \cdot 10^{-3} \tag{18}$$

Eq. 18 is used in the Spectral Wave Model Nearshore (SWAN) with strong wind effect taken into consideration.

Upon the availability of stability data z/L from GWA III through mesoscale WRF modeling (with a spatial resolution of 3 km), the algorithms are also adjusted to take the stability effect into account. Since at a particular point, the z/L data are only 7 numbers with occurrence frequency, the adjustification of the algorithms implements a decreasing stability effect from low-moderate wind speed to strong speed, meaning that it becomes neutral at U reaching 25 ms^{-1}. The effect shows to be dominating and an additional coefficient is used to weaken this effect brought in from the 3 km WRF modeling. When compared with measurements, it suggests that the uncertainty related to this input of z/L is significantly bigger than the value it brings. Until a more reliable stability data becomes available, our calculation continues with $z/L = 0$. Though the algorithms allow individual input of z/L, which in case of special occasions (e.g. a measurement site) can be applied.

4.2 Shear-based turbulence with stability

A simple model is derived to get mean σ_u based on a statistical ('equilibrium') form of the non-dimensional TKE budget. Following Kelly et al. (2014), it is essentially a non-dimensional extension of local-similarity theory (consistent with e.g. Nieuwstadt, 1984), plus terrain-induced turbulent transport (engineering hybrid between Kelly et al. (2009) and Hatlee and Wyngaard (2007) forms and the IEC (2019) prescription). Its equation is

$$\langle\sigma_u\rangle = \frac{\langle\alpha\rangle\langle U\rangle + TX}{1 + z \times (L^{-1})_{\mathrm{eff}}}\,. \tag{19}$$

Analogous to WAsP's treatment and M-O functions, the stability damping or enhancement of turbulence is also functionally constrained (within the `zinvLeff` function, $z \times (L^{-1})_{\mathrm{eff}}$ in the equation above); the long-term effective stability depends on the mean and standard deviation of inverse Obukhov length (Kelly and Gryning, 2010; Kelly and Troen, 2016). Noting that the α input from LINCOM is a neutral "version", it must be compensated; this is done with a form following from Kelly et al. (2014) and Kelly et al. (2019), amenable to perturbed flow above the surface layer. Terrain enhancement of turbulence is found in the horizontal turbulent-transport term (TX) of the dimensionless TKE budget.

To conform to the IEC 61400-1 prescription, in (19) TX is parameterized such that it can also be cast as a factor multiplying $\langle\alpha\rangle\langle U\rangle$; expressed as a multiplier of the main part ($(\langle\alpha\rangle\langle U\rangle)$), the terrain-complexity component of TX can range between 1 and 1.4–thus offering 15% increase per the IEC, with partial safety factor of 1.2. Two crude empirical forms for sector-wise terrain-enhancement (TX) are given: one based on directional RIX (per sector), and the other based on terrain-inclination angle. Both also use z_0, to account for the turbulence augmentation due to forest, etc.

[Note that this Mean $\langle\sigma_u\rangle$ estimate has less uncertainty than the two coefficients of a linear $\sigma_u = A_\sigma U + B_\sigma$ form with linear U-dependence.]

Compared to v1, this version has an update to estimate A_σ, B_σ, with A_σ now including a dependence on $\langle\sigma_u\rangle$. There are 2 tunable parameters (if we or EMD wish to optimize), which can vary between 0 and 1. If the first parameter (c_s) is set to 0 and the second (d_s) set to 0.75, then the v1 form is recovered. The new form $\sigma_u(U)$ is made such that taking its mean, one recovers $\langle\sigma_u\rangle$ regardless of the values of c_s and d_s.

For EMD's load estimates, I also give an estimator for the $\sigma_{u90\%}$, i.e. the 90th percentile σ_u that is used in the IEC standard (which replaced the earlier σ_{σ_u} and 'CTI' from ed.2).

It takes the estimated $\langle\sigma_u\rangle$ from (19) as input, and has a slight roughness dependence which comes via the parameter x (consistent with log-normal or Weibull in ed.3 or ed.4):

$$\langle\sigma_{u90\%}\rangle \approx (C_{90}\langle\sigma_u\rangle)^x \ , \ x \equiv 1 - c_1\{1 + \tanh[\ln(z_0/z_{0ick})]\} \tag{20}$$

with c_1 chosen as 0.1 and C_{90} ≈1.8-2.2. Also the roughness scale $z_{0ick} = 0.1$m is the same as in the formulation/code for σ_u. So the exponent x varies from 1 for typical roughnesses down to ∼0.8 for forest.

A simple extension is put on to include the U-dependence, consistent with (and using) the roughness-dependence in $\langle\sigma_{u90}\rangle$ above: * $\sigma_{u90\%}(U) \approx \langle\sigma_{u90\%}\rangle[1 + c_{A90}(U/\langle U\rangle - 1)]$

using c_{A90} ≈0.5 to 1 depending on the TX parameterization and fidelity(resolution) of the α input; it might need to be adjusted/tuned.

4.3 The ensemble

An average of the estimates from the two approaches gives smaller bias when compared with measurements. It is the average of this small ensemble that is used for the final estimate.

5 Extreme winds over water at 50 m, 100 m and 150 m

To calculate extreme winds over water at height z =50 m, 100 m and 150 m with winds at 10 m from the CFSR data, very simple approach is taken. First, the logarithmic wind law is applied:

$$U_z = (u_*/\kappa)\ln(z/z_0). \tag{21}$$

With U_{10m} at $z = 10$ m known, one more equation for z_0 and u_*, U_z can thus be obtained analytically.

As also described in Larsén and Ott (2020), three approaches are used to obtain the relation between z_0 and u_*, we call them

- Charnock (Charnock, 1955)

- AE (Andreas E.) (Andreas et al., 2015)
- SWAN (Zijlema and van der Westhuysen, 2005)

For the Charnock formulation,

$$z_0 = \alpha_{ch} u_*^2 / g$$

where α_{ch} is the Charnock coefficient, which depends on the sea state. In WRF, it is a function of wind speed, increasing from 0.011 to about 0.02 at strong winds. The correction is done to annual wind maxima, therefore we use $\alpha_{ch} = 0.02$.

For the AE formulation, the wave breaking effect is embedded in the description of u_*

$$u_* = 0.239 + 0.0433((U_{10m} - 8.271) + (0.12(U_{10m} - 8.271)^2 + 0.181)^{0.5})$$
$$z_0 = 10 \exp(-\kappa U_{10m}/u_*) \tag{22}$$

For the SWAN formulation, the surface conditions at strong winds are also taken into consideration

$$C_d = (0.55 + 2.97(U_{10m}/31.5) - 1.49(U_{10m}/31.5)^2) 10^{-3}$$
$$u_* = \sqrt{C_d} U_{10m}$$
$$z_0 = 10 \exp(-\kappa U_{10m}/u_*) \tag{23}$$

This is the same as used for turbulence modeling over water grids in section 4.1.

The 10-m wind speed in the range from 1 to 50 ms^{-1} is extrapolated to 100 m using the above three approaches and the results are compared in Fig. 7. There is basically no difference between the three methods for winds up to 25 ms^{-1}. The Charnock with $\alpha_{ch} = 0.02$ gives very similar results to the AE algorithm. The difference between the SWAN and the other two becomes noticeable from 25 to about 40 ms^{-1}, and becomes non-negligible for $U_{100m} > 40$ ms^{-1}. Seemingly, The simplification of using $\alpha_{ch} = 0.02$ is not a problem when compared with the AE algorithm, though it might have caused the overestimation of strongest winds when compared with the SWAN algorithm.

We use the SWAN algorithms for the final calculation.

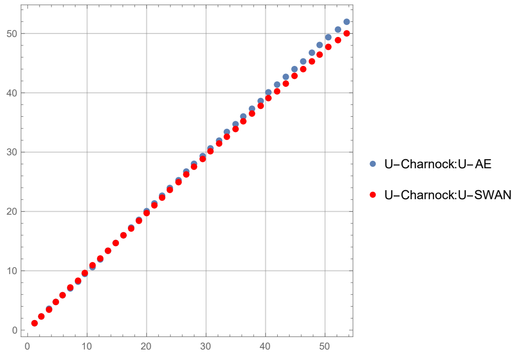

Figure 7: Comparison of extrapolated winds at 100 m from 10 m using the three methods for u_* and z_0 over water.

6 Extreme winds in tropical cyclone affected water area

The calculation is briefly introduced here, please refer to Larsén and Ott (2020) for details. We continue using CFSR data and the spectral correction method, though with adjust for the tropical cyclone affected area. In connection with the spectral correction, the following spectral model was used

$$fS(f) = n(a_1 f^{-2/3} + a_2 f^{-2}) \tag{24}$$

For the calculations in section 2.5, $n = 1$. Here n is obtained as a function of wind speed, as calibrated using the Best Track data from Ott (2005) and the estimation from CFSR data (see Larsén and Ott (2020)).

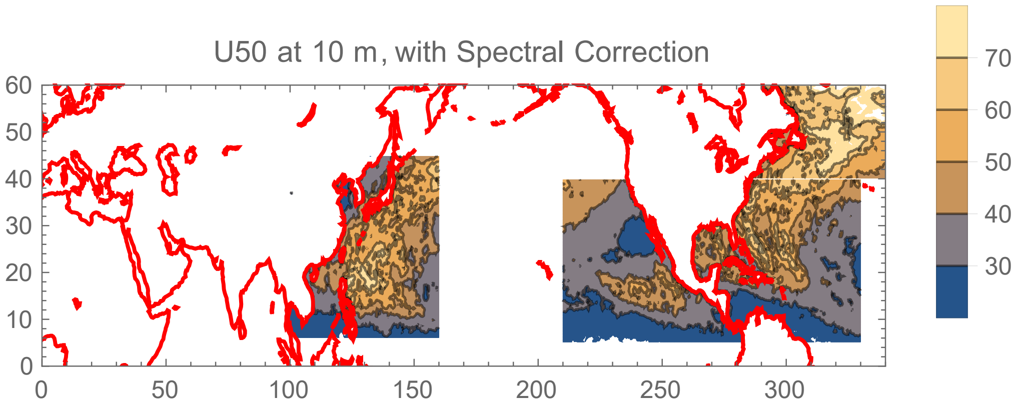

Figure 8: Spatial distribution of U_{50} with spectral correction for Hurricanes using n.

Both the Charnock formulation and the SWAN formulation are used to the annual maximum wind at 10 m to obtain the corresponding values at 50 m, 100 m and 150 m for data in the area as shown in Fig. 8.

7 Grid tiling

The GASP output was produced on a global latitude-longitude grid. To facilitate the calculations, a tiling of the globe was made on several levels:

1. The global latitude-longitude grid was constructed with a spacing of 1/400 degrees (≈ 275 m).
2. The globe was split into 6x8 degree zones with a column identifier (number) corresponding to UTM zones and a row identifier (letter) similar to the Military Grid Reference System (MGRS) grid. However, for convenience the exceptions of MGRS (e.g. in Norway and in the polar regions) were not used. Figure 9 shows the 751 relevant zones. The zones left out do not contain any land or coastal (200 km offshore) area.
3. For each zone, a number of calculation grids were defined in the corresponding UTM projection, shown for zone 29U in Fig. 10 (a). Each calculation grid is of size 800×800 with spacing of 125 m and overlaps on the edge by it's neighbour grid-edges.
4. A secondary latitude-longitude tiling was made in parallel to the zones, shown in Fig. 10 (b). These are smaller than the zones and are meant to store results in smaller chunks than a whole zone.

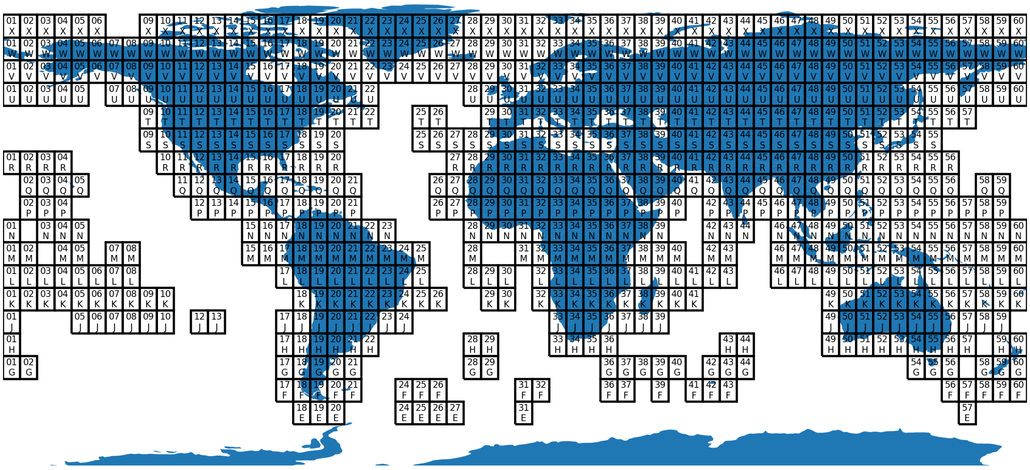

Figure 9: GASP zones 6x8 degree large. Mostly equal to MGRS zones, but with no locally altered zones (e.g. zone 32V).

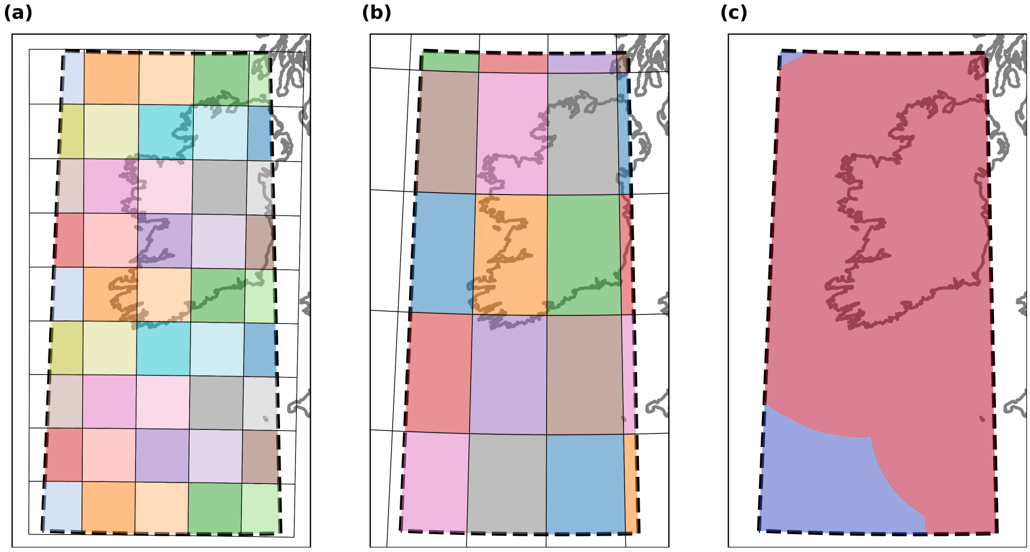

(a) **(b)** **(c)**

Figure 10: Tiling of GASP zone 29U (dashed black line) covering Ireland to the north. **(a)**: Calculation grids (boxes) in local UTM projection. The colored part of the boxes highlights the areas of each grid within the GASP zone 29U. **(b)**: output tiles (colored boxes) in latitude-longitude projection. **(c)**: Calculation mask (red=calculate, blue=do not calculate) corresponding to land masks and a region extending 200 km offshore.

7.1 Inclusion zone

A global land mask based on the Global Self-consistent, Hierarchical, High-resolution Geography Database (GSHHG; Wessel and Smith, 1996) was used to limit the calculations to land and coastal areas. The mask was buffered to extend 200 km offshore. Figure 10 (C) shows an example of the inclusion zone for the GASP zone 29U.

8 Datasets

The datasets of terrain, elevation, land cover are introduced in the project report D1.1, here as Appendix a.

9 Preliminary results

Figure 11 shows the global distribution of the 50-year wind at 100 m, at the spatial resolution of 250 m, in similar manner as the Global Wind Atlas.

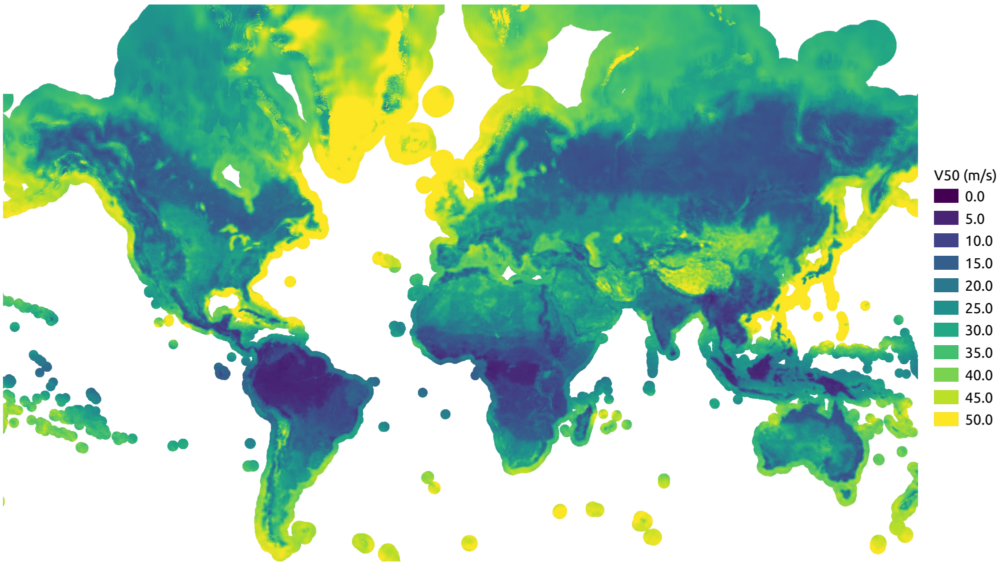

Figure 11: The global atlas of the 50-year wind at 100 m, at a spatial resolution of 250 m.

References

Abild, J. (1994). *Application of the wind atlas method to extremes of wind climatology*. Number 722(EN) in Denmark. Forskningscenter Risoe. Risoe-R.

Andreas, E. L., Mahrt, L., and Vickers, D. (2015). An improved bulk air-sea surface flux algorithm, including spray-mediated transfer. *Q.J.R. Meteorol. Soc.*, 141:642–654.

Astrup, P., Jensen, N., and Mikkelsen, T. (1996). *Surface roughness model for LINCOM*. Number 900(EN) in Denmark. Forskningscenter Risoe. Risoe-R.

Badger, J., Frank, H., Hahmann, A. N., and Giebel, G. (2014). Wind-climate estimation based on mesoscale and microscale modeling: Statistical-dynamical downscaling for wind energy applications. *Journal of Applied Meteorology and Climatology*, 53(8):1901–1919.

Charnock, H. (1955). Wind stress on a water surface. *Q. J. R. Meteorol. Soc.*, 81:639–640.

Floors, R. and Nielsen, M. (2019). Estimating Air Density Using Observations and Re-Analysis Outputs for Wind Energy Purposes. *Energies*, 12(11):2038.

Hansen, B. O., LarsÃ©n, X. G., Kelly, M., Rathmann, O. S., Berg, J., Bechmann, A., Sempreviva, A. M., and JÃ¸rgensen, H. E. (2016). Extreme wind calculation applying spectral correction method - test and validation. Technical report, Wind Enery Department, Technical University of Denmark, DTU Wind Energy E-0098.

Hatlee, S. C. and Wyngaard, J. C. (2007). Improved subfilter-scale models from the HATS field data. *Journal of the Atmospheric Sciences*, 64(5):1694–1705.

IEC (2019). IEC 61400-1 Ed4: Wind turbines - Part 1: Design requirements. standard, International Electrotechnical Commission, Geneva, Switzerland.

Kaimal, J., Wyngaard, J., Izumi, Y., and CotÃ©, O. (1972). Spectral characteristics of surface-layer turbulence. *Q. J. R. Meteorol. Soc*, 98:563–589.

Kelly, M. and Gryning, S.-E. (2010). Long-term mean wind profiles based on similarity theory. *Boundary-Layer Meteorology*, 136(3):377–390.

Kelly, M., Kersting, G., Mazoyer, P., Yang, C., Fillols, F. H., Clark, S., and Matos, J. C. (2019). Uncertainty in vertical extrapolation of measured wind speed via shear. Technical Report E-0195(EN), Wind Energy Dept., Risø Lab/Campus, Danish Tech. Univ. (DTU), Roskilde, Denmark.

Kelly, M., Larsen, G., Dimitrov, N. K., and Natarajan, A. (2014). Probabilistic meteorological characterization for turbine loads. *Journal of Physics: Conference Series*, 524(1):012076.

Kelly, M. and Troen, I. (2016). Probabilistic stability and "tall" wind profiles: theory and method for use in wind resource assessment. *Wind Energy*, 19(2):227–241.

Kelly, M., Wyngaard, J. C., and Sullivan, P. P. (2009). Application of a subfilter-scale flux model over the ocean using OHATS field data. *Journal of the Atmospheric Sciences*, 66(10):3217–3225.

Larsén, X., Davis, N., Olsen, B., and Floors, R. (2019). On the database of global reanalysis wind, terrain, land cover and observations. *GASP technical reports D1.1.*

Larsén, X. and Mann, J. (2009). Extreme Winds from the NCEP/NCAR Reanalysis Data. *Wind Energy*, 12(6):556–573.

Larsén, X. and Ott, S. (2020). Extreme winds in tropical cyclone affected water areas. Technical Report DTU Wind Energy E-0206, ISBN 978-87-93549-74-6, DTU Wind Energy Department.

Larsén, X. G. and Kruger, A. (2014). Application of the spectral correction method to reanalysis data in South Africa. *J. Wind Eng. Ind. Aerodyn.*, 133:110–122.

Larsén, X. G., Ott, S., Badger, J., Hahmann, A. N., and Mann, J. (2012). Recipes for correcting the impact of effective mesoscale resolution on the estimation of extreme winds. *Journal of Applied Meteorology and Climatology*, 51(3):521–533.

Nieuwstadt, F. T. M. (1984). The turbulent structure of the stable, nocturnal boundary layer. *Journal of the Atmospheric Sciences*, 41(14):2202–2216.

Ott, S. (2005). Extreme winds in the western North Pacific. Technical Report Risoe-R-1544(EN), RisÃ¸ National Laboratory, Roskilde, Denmark, URL:www.risoe.dk/rispubl/VEA/veapdf/ris-r-1544.pdf.

Saha, S., Moorthi, S., Pan, H.-L., Wu, X., Wang, J., Nadiga, S., Tripp, P., Kistler, R., Woollen, J., Behringer, D., Liu, H., Stokes, D., Grumbine, R., Gayno, G., Wang, J., Hou, Y.-T., Chuang, H.-Y., Juang, H.-M. H., Sela, J., Iredell, M., Treadon, R., Kleist, D., Delst, P. V., Keyser, D., Derber, J., Ek, M., Meng, J., Wei, H., Yang, R., Lord, S., van den Dool, H., Kumar, A., Wang, W., Long, C., Chelliah, M., Xue, Y., Huang, B., Schemm, J.-K., Ebisuzaki, W., Lin, R., Xie, P., Chen, M., Zhou, S., Higgins, W., Zou, C.-Z., Liu, Q., Chen, Y., Han, Y., Cucurull, L., Reynolds, R. W., Rutledge, G., and Goldberg, M. (2010). NCEP climate forecast system reanalysis (CFSR) selected hourly time-series products, January 1979 to December 2010.

Troen, I. and Petersen, E. L. (1989). *European Wind Atlas*. RisÃ¸ National Laboratory, Roskilde, Denmark, ISBN 87-550-1482-8, 656 pp, http://orbit.dtu.dk/files/112135732/European_Wind_Atlas.pdf.

Wessel, P. and Smith, W. H. F. (1996). A global, self-consistent, hierarchical, high-resolution shoreline database. *J. Geophys. Res.*, 101(B4):8741–8743.

Zijlema, M. and van der Westhuysen, A. J. (2005). On convergence behaviour and numerical accuracy in stationary SWAN simulations of nearshore wind wave spectra. *Coastal Engineering*, 52(3):237–256.